

# Reconstruction from Multiple Particles for 3D Isotropic Resolution in Fluorescence Microscopy

Denis Fortun, Paul Guichard, Virginie Hamel, Carlos Oscar S. Sorzano, Niccolò Banterle, Pierre Gönczy, and Michael Unser

**Abstract**—The imaging of proteins within macromolecular complexes has been limited by the low axial resolution of optical microscopes. To overcome this problem, we propose a novel computational reconstruction method that yields isotropic resolution in fluorescence imaging. The guiding principle is to reconstruct a single volume from observations of multiple rotated particles. Our new operational framework detects particles, estimates their orientation, and reconstructs the final volume. The main challenge comes from the absence of initial template and *a priori* knowledge about the orientations. We formulate the estimation as a blind inverse problem, and propose a block-coordinate stochastic approach to solve the associated non-convex optimization problem. The reconstruction is performed jointly in multiple channels. We demonstrate that our method is able to reconstruct volumes with 3D isotropic resolution on simulated data. We also perform isotropic reconstructions from real experimental data of doubly labelled purified human centrioles. Our approach revealed the precise localization of the centriolar protein Cep63 around the centriole microtubule barrel. Overall, our method offers new perspectives for applications in biology that require the isotropic mapping of proteins within macromolecular assemblies.

**Index Terms**—Protein localization, isotropic resolution, image reconstruction, pose estimation, multichannel fluorescence.

## I. INTRODUCTION

Establishing a map of the position of proteins or other sub-macromolecular components within large macromolecular assemblies and organelles is crucial to fully understand their function. However, due to their small size, most studies of such complexes have been carried using electron microscopy (EM) [23], which can resolve their ultrastructure but does not allow to readily determine the position of specific components thereof, except via labor intensive immuno-electron microscopy methods [28]. Meanwhile, proteins can be localized in fluorescence imaging with various techniques, including direct immunofluorescence, fluorescent proteins such as GFP,

D. Fortun is with the Signal Processing core of Center for Biomedical Imaging (CIBM-SP), EPFL, Lausanne, Switzerland.

P. Guichard and V. Hamel were with the Swiss Institute for Experimental Cancer Research (ISREC), School of Life Sciences, Swiss Federal Institute of Technology (EPFL), 1015 Lausanne, Switzerland. They are now with the Department of Cell Biology, University of Geneva, Sciences III, Geneva, Switzerland.

C.O.S. Sorzano is with the Biocomputing Unit, National Center for Biotechnology (CSIC), Madrid, Spain, and the Bioengineering Lab, Universidad CEU San Pablo, Madrid, Spain.

N. Banterle and P. Gönczy are with the Swiss Institute for Experimental Cancer Research (ISREC), School of Life Sciences, Swiss Federal Institute of Technology (EPFL), 1015 Lausanne, Switzerland.

M. Unser is with Biomedical Imaging Group, EPFL, Lausanne, Switzerland.

This project has received funding from the European Research Council (ERC) under the European Unions Horizon 2020 research and innovation programme (GA No 692726 GlobalBioIm)

self-labeling enzymes, enzymes that catalyze the attachment of a probe to a target sequence, or biarsenical dyes that target tetracysteine motifs (see [13] for a review). However, despite the high-accuracy of super-resolution methods in the lateral plane [5], [27], [40], their low axial resolution still severely limits the accuracy of 3D imaging [22]. This anisotropy can be reduced only partially by optical methods [26], [36].

We propose here an image reconstruction framework that makes the axial resolution match that of the lateral plane. Moreover, we provide a means to localize sub-macromolecular components by handling multicolor imaging to combine architectural and protein information in different channels. Input volumes contain multiple replicates of a macromolecular assembly with different orientations, acquired with a super-resolution microscope. The macromolecular assembly is stained with multiple fluorophores, each corresponding to the distribution of one protein species. We exploit the different details provided by each view to reconstruct a common 3D multichannel model with isotropic resolution that represents the relative position of the proteins. Three main tasks have to be realized: 1) Detection of the particles in the input volumes; 2) Estimation of the orientation of each particle; 3) Reconstruction of a common multichannel model. In previous work [19], we developed a method to address the third task and have already demonstrated the feasibility of the reconstruction for a large number of input particles. This proof of concept was realized merely on simulated data for a single channel, without particle detection and assuming known orientations.

In this paper, by contrast, we propose a method that combines all three tasks. We focus on modalities where image acquisition can be modeled by a convolution with a point spread function (PSF), such as STED or confocal imaging. The detection is based on a semi-automatic learning strategy using a few training examples that are picked manually. The estimation of the orientations and the single volume reconstruction are performed jointly without initial template. This is the most crucial and challenging step. We formulate it as a semi-blind inverse problem that involves a non-convex optimization task. We solve it in two steps.

In the first step, we propose a bilevel optimization framework based on stochastic optimization, which ensures robustness to local minima. To deal with the computational challenge that results from the large amount of 3D data, we reduce the complexity of the problem by particle clustering and we integrate the estimation in a block-coordinate scheme. In the second step, we refine the results with fast alternated optimization to obtain high-accuracy results.

We first validate experimentally the performance of our

method on realistic simulated data. Then, we challenge the method on real experimental data. We reveal the localization of the protein Cep63 around the centriole barrel. Overall, our method opens a large range of perspectives for the mapping of sub-macromolecular components.

Our contributions can be summarized as follows:

- Design of a complete operational framework for the reconstruction of a volume with isotropic resolution from multiple particles in 3D multichannel fluorescence microscopy.
- Fast and robust block-coordinate stochastic optimization method to solve the non-convex problem of joint pose estimation and reconstruction of a common model. The main advantage of our method is to be template-free, with a low computational cost even for large 3D datasets.
- Demonstration of the accuracy of protein localization with our method, both on simulated and real data.

### A. Related Work

The problem of protein mapping has been addressed by correlative light-and electron-microscopy (CLEM) [14], and by combining structured illumination microscopy (SIM) with single molecule localization microscopy (SMLM) [24]. However, both approaches do not address the low axial resolution issue. The other major issue in CLEM is the co-registration of different imaging modalities using either physical landmarks in the sample [25] or manual assignment of correspondences [29]. Furthermore, the accuracy of automatic registration techniques [2], [10] depends on the presence of salient image features, which are not always available.

Particle averaging methods with 2D alignment have been explored for fluorescence images [31], [41], [42]. However, the anisotropic nature of the PSF has been taken into account only by 3D averaging methods in SIM [9], [33] and SMLM [8]. These works have yielded isotropic resolution, but they are limited by two main points. Firstly, the estimation of orientations requires a prior template model onto which particles are registered, which simplifies the problem but causes a strong bias in the reconstruction. Secondly, they perform an average of particles that produces blurring artefacts. We highlighted this effect and how to reduce it with sparsity-based reconstruction [19].

By contrast, the single-particle analysis framework in cryo-electron microscopy (cryo-EM) reconstructs a single particle without knowledge of the poses [11]. However, the imaging model of cryo-EM is a 2D projection obtained through the Radon transform, which fundamentally differs from the present convolutional model in fluorescence microscopy. Moreover the samples must be frozen and only the architecture of the macromolecular assembly can be imaged in cryo-EM, precluding multichannel acquisition and, thus, allocation of specific protein localizations.

While resolution improvement in fluorescence imaging is usually performed by single view deconvolution [16], [17], other techniques based on multiviews have been proposed, such as 3D total-internal reflection fluorescence microscopy [7], selective plane illumination microscopy [38], [43], optical

projection tomography [6], [12], optical coherence tomography [6], and fluorescence molecular tomography [3]. However, these methods have access to an accurate *a priori* knowledge of the orientations, and their resolution is not isotropic.

### B. Organization of the Manuscript

We describe the global structure of our method and its main steps in Section II. In Section III, we detail the joint pose estimation and volume reconstruction, without initial reference. In Section IV, we focus on the subsequent step, where the previous estimation is refined. In Section V, we evaluate the performance on simulated and real data.

## II. RECONSTRUCTION FRAMEWORK

The overall organization of our framework is sketched in Figure 1. The primary steps are (1) *particle detection*, (2) *reference-free reconstruction*, and (3) *high-accuracy reconstruction*. Steps (2) and (3) will be described in more details in Sections III and IV.

### A. Input Data

The input data are a set of multichannel volumes that contain several replicates of the same macromolecular assembly. In our approach, we assume that the particles are identical and exhibit random orientations. We model the image acquisition by a linear convolutional forward model. Each channel allows monitoring of a different protein of interest, with one channel aimed at describing the structure of the particle and another one (or other ones) aimed at determining the precise localization of a given protein in that structure. As can be seen in Figure 1, the details of the particles are much blurred in the axial direction (XZ and ZY planes), while they are preserved and observed in different orientations in the lateral XY plane. The goal is to produce a single model of the particle by exploiting the high lateral resolution of the different views.

### B. Particle Detection

The first step is to detect and extract particles from the input volumes. To avoid errors of fully automatic detection and tedious manual picking, we adopt a semi-automatic approach. Firstly, a few particles are manually selected in a region of interest of the input volumes to train a classifier. Then the other particles are automatically detected based on the learned features.

To facilitate manual picking by the user, we first build 2D images as the maximum-intensity projection of the volume along the axial direction. The 2D manual picking is realized with the interface of the Scipion software [15], and is then extended in the axial direction.

Our training and classification steps follow the approach described in [1]. In brief, cascaded support vector machine classifiers are trained with features calculated at the particle locations while negative examples are taken from the background of the micrograph. All these features, about 90, are used to classify data as particle or background.

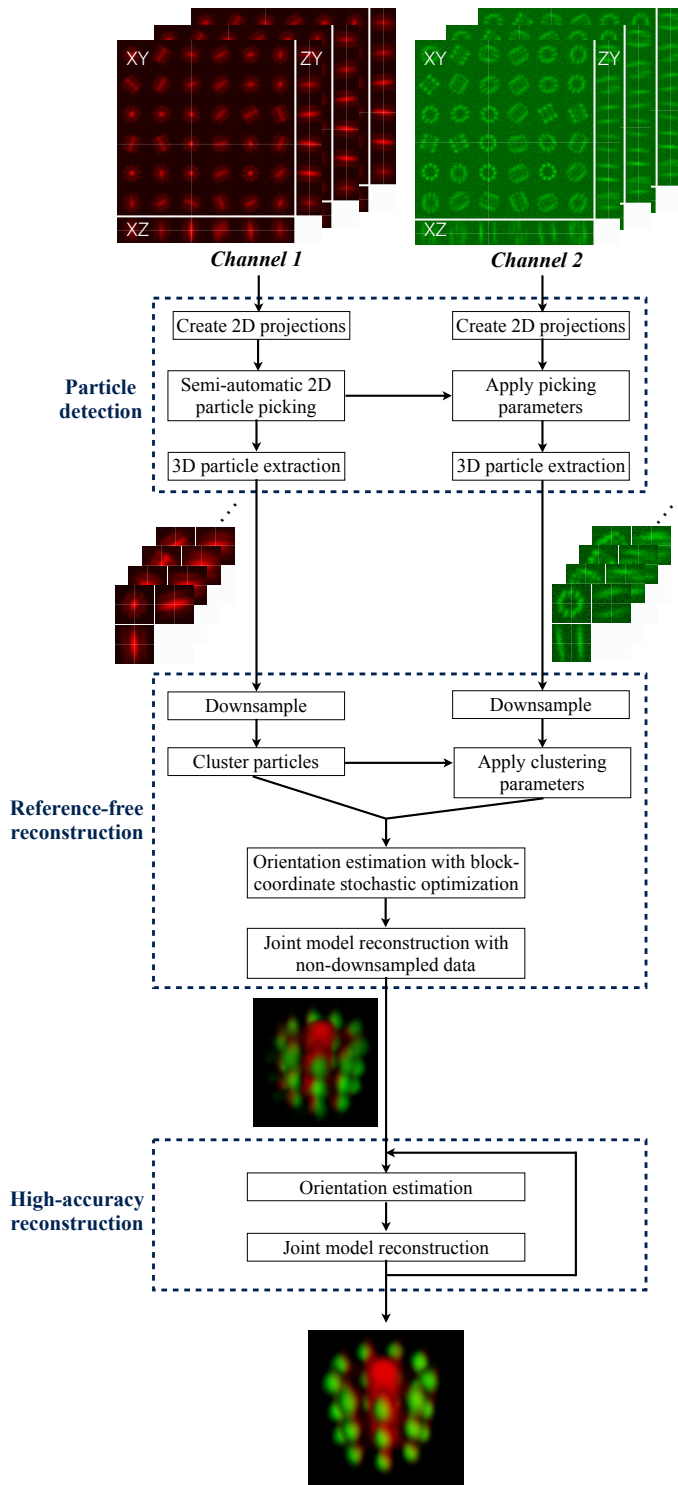


Fig. 1. Block diagram of our reconstruction framework.

The particle detection is performed in a single channel chosen by the user, and is then propagated to the other channels.

### C. Joint Single Volume Reconstruction and Pose Estimation

The particle detection step provides a set of multichannel volumes that contain individual particles. These particles may

have different orientations and different shifts with respect to the center of the volumes. The volume reconstruction and pose estimation are dependent on each other and have to be realized jointly.

To formalize the problem, let us denote in vector notation  $\mathbf{x} \in \mathbb{R}^{N \cdot N_c}$  the common multichannel fluorescence model, where  $N$  is the number of voxels and  $N_c$  is the number of channels. The pose associated to the  $i$ th particle is denoted  $\vartheta_i = (\mathbf{t}_i, \boldsymbol{\theta}_i) \in \mathbb{R}^6$  and is composed of the 3D translation  $\mathbf{t}_i$  and of three Euler rotation angles collected in  $\boldsymbol{\theta}_i$ . We define the aligned particle  $\mathbf{y}_{\vartheta_i} \in \mathbb{R}^{N \cdot N_c}$  as the  $i$ th detected volume on which the inverse rotation of angle  $\boldsymbol{\theta}_i$  and the translation  $(-\mathbf{t}_i)$  have been applied. We model the image acquisition process by the convolution of the signal with a point-spread function (PSF). We denote by  $\bar{\mathbf{H}}_{\vartheta_i}$  the block-diagonal matrix defined by  $\bar{\mathbf{H}}_{\vartheta_i} = \text{diag}(\mathbf{H}_{\vartheta_i}^1, \dots, \mathbf{H}_{\vartheta_i}^{N_c})$ , where  $\mathbf{H}_{\vartheta_i}^c \in \mathbb{R}^{N \times N}$  is the PSF matrix of the channel indexed by  $c$  on which the inverse rotation of angle  $\boldsymbol{\theta}_i$  has been applied. Then, the acquisition model for each aligned particle can be written (see [19] for a continuous derivation)

$$\mathbf{y}_{\vartheta_i} = \bar{\mathbf{H}}_{\vartheta_i} \mathbf{x}. \quad (1)$$

To reconstruct the common model  $\mathbf{x}$ , we have to solve a semi-blind inverse problem where the parameter  $\vartheta_i$  of the forward model is unknown. We estimate jointly  $\mathbf{x}$  and  $\boldsymbol{\vartheta} = (\vartheta_1, \dots, \vartheta_K)$ , where  $K$  is the number of particles, by solving the minimization problem

$$\{\hat{\mathbf{x}}, \hat{\boldsymbol{\vartheta}}\} = \arg \min_{\mathbf{x} \in \mathbb{R}_+^{N \cdot N_c}, \boldsymbol{\vartheta} \in \mathbb{R}^{K \times 6}} \sum_{i=1}^K \|\mathbf{y}_{\vartheta_i} - \bar{\mathbf{H}}_{\vartheta_i} \mathbf{x}\|_2^2 + \lambda \|\mathbf{D}\mathbf{x}\|_p^p, \quad (2)$$

where  $\mathbf{D}$  is the first order finite-difference matrix and  $p \in \{1, 2\}$ . The first term promotes data fidelity by penalizing deviations from the forward model (1) under the assumption of Gaussian noise. The second term is a regularization that favors smoothness or piecewise-constant solutions. The choice of  $p$  will be discussed in Sections III and IV.

The difficulty of the joint optimization problem (2) lies in its high non-convexity. It is not biconvex either since the minimization w.r.t.  $\mathbf{x}$  with  $\boldsymbol{\vartheta}$  fixed is convex, but the minimization w.r.t.  $\boldsymbol{\vartheta}$  with  $\mathbf{x}$  fixed is itself strongly non-convex. In this situation, an alternated optimization scheme w.r.t.  $\mathbf{x}$  and  $\boldsymbol{\vartheta}$  is not guaranteed to converge to a global minimum. If convergence conditions are met for the two subproblems [4], [47], the joint problem can converge to a local optimum. In practice, the algorithmic solution will highly depend upon the initialization. To overcome this issue, we propose a robust preliminary reconstruction step without initialization. We call this step *reference-free* reconstruction (cf. Figure 1). The resulting volume is refined in the *high-accuracy* reconstruction step by fast alternated optimization. The reconstruction is performed jointly in all the channels. We detail these two steps in Sections III and IV.

## III. REFERENCE-FREE RECONSTRUCTION

### A. Stochastic Optimization

The goal of the *reference-free* reconstruction is to produce an initial model appropriate for subsequent refinement. Thus,

our foremost aim here is serviceability rather than high-accuracy. The general idea is to design a stochastic optimization strategy that is adapted to non-convex objective functions while remaining computationally tractable.

To that end, we reduce the complexity of the original problem as follows.

- Firstly, we downsample the input volumes. We empirically found volumes of size  $30^3$  voxels to be a good compromise between accuracy and computational cost.
- Secondly, we reduce the initial number  $K$  of particles used for the reconstruction. The particles are carefully selected to preserve most of the information and avoid redundant orientations. This reduction is achieved by classifying the particles in  $L$  labels with a k-means algorithm, such that each class regroups particles with similar orientations. We keep only the particle closest to the centroid in each class.
- Thirdly, we consider a quadratic regularization model by setting  $p = 2$  in (2). The advantage of the quadratic model is that the optimization of (2) w.r.t.  $\mathbf{x}$  can be solved analytically and implemented very efficiently in the Fourier domain.

Accordingly, we reformulate the joint optimization problem (2) in the bilevel form

$$\hat{\boldsymbol{\vartheta}} = \arg \min_{\boldsymbol{\vartheta} \in \mathbb{R}^{L \times 6}} E(\hat{\mathbf{x}}(\boldsymbol{\vartheta}), \boldsymbol{\vartheta}) \quad (3)$$

$$\text{s.t. } \hat{\mathbf{x}}(\boldsymbol{\vartheta}) = \arg \min_{\mathbf{x} \in \mathbb{R}_+^{N \cdot N_c}} E(\mathbf{x}, \boldsymbol{\vartheta}) \quad (4)$$

where  $E(\mathbf{x}, \boldsymbol{\vartheta}) = \sum_{i=1}^L \|\mathbf{y}_{\boldsymbol{\vartheta}_i} - \bar{\mathbf{H}}_{\boldsymbol{\vartheta}_i} \mathbf{x}\|_2^2 + \lambda \|\mathbf{D}\mathbf{x}\|_2^2$ . Thanks to the simplified setting described above, the computation of  $\hat{\mathbf{x}}(\boldsymbol{\vartheta})$  is fast and exact, so that the energy  $E(\hat{\mathbf{x}}(\boldsymbol{\vartheta}), \boldsymbol{\vartheta})$  in (3) can be evaluated efficiently for a given  $\boldsymbol{\vartheta}$ . This makes it feasible to minimize the problem (3) w.r.t.  $\boldsymbol{\vartheta}$  with a stochastic optimization method based on randomized search in the space of admissible rotations, despite the large number of required evaluations of the cost functional. The randomization enables one to escape local minima. While stochastic optimization such as simulated annealing is known to be slow for large dimensions (*e.g.*, when the parameters are image pixels), it is well adapted in our case because of the reduction of the number of particles, the downsampling of the input volumes, and our quadratic model.

In a probabilistic framework, Problem (3) can be formulated as the maximum-likelihood estimation of  $\boldsymbol{\vartheta}$ , where the likelihood of  $\boldsymbol{\vartheta}$  for  $\mathbf{x}$  fixed is given by  $p(\mathbf{y}|\boldsymbol{\vartheta}) = e^{-E(\mathbf{x}, \boldsymbol{\vartheta})}/Z$ ,  $\mathbf{y} = (\mathbf{y}_{\boldsymbol{\vartheta}_1}, \dots, \mathbf{y}_{\boldsymbol{\vartheta}_k})$ , and where  $Z$  is a normalization constant. To maximize  $p(\mathbf{y}|\boldsymbol{\vartheta})$ , we follow a Monte-Carlo Markov-chain (MCMC) approach by generating the sequence  $(\boldsymbol{\vartheta}^{(n)})_{n \geq 0}$  of random variables with a Metropolis-Hastings algorithm [37]. To force convergence of the chain to the maximum value of  $p(\mathbf{y}|\boldsymbol{\vartheta})$ , we apply an annealing procedure on the energy  $E(\mathbf{x}, \boldsymbol{\vartheta})$  [20]. At iteration  $t$ , the main steps of the method are

- 1) Randomly generate a candidate orientation vector  $\tilde{\boldsymbol{\vartheta}} = (\tilde{\boldsymbol{\vartheta}}_1, \dots, \tilde{\boldsymbol{\vartheta}}_L)$  defined as  $\tilde{\boldsymbol{\vartheta}}_i = \boldsymbol{\vartheta}_i^{(t-1)} + \mathbf{w}_i$ , where  $\mathbf{w}_i \sim \mathcal{N}(\mathbf{0}, \boldsymbol{\sigma})$ ,  $\boldsymbol{\sigma} \in \mathbb{R}_+^6$ .
- 2) Compute the cost function  $E(\hat{\mathbf{x}}(\tilde{\boldsymbol{\vartheta}}), \tilde{\boldsymbol{\vartheta}})$  associated with the candidate.

### Algorithm 1 Simulated annealing procedure

---

Set random initial values to  $\boldsymbol{\vartheta}$ ,  $t = 1$   
**while** stopping criterion not met **do**  
 $\forall i \in [1, \dots, L]$ , Draw  $\tilde{\boldsymbol{\vartheta}}_i = \boldsymbol{\vartheta}_i^{(t-1)} + \mathbf{w}_i$ ,  $\mathbf{w}_i \sim \mathcal{N}(\mathbf{0}, \boldsymbol{\sigma})$   
 $\tilde{\mathbf{x}} = \mathcal{F}^{-1} \left\{ \frac{\sum_{i=1}^L \mathcal{F}\{\mathbf{H}_{\tilde{\boldsymbol{\vartheta}}_i}^\top \mathbf{y}_{\tilde{\boldsymbol{\vartheta}}_i}\}}{\sum_{i=1}^L |\mathcal{F}\{\mathbf{H}_{\tilde{\boldsymbol{\vartheta}}_i}\}|^2 + \lambda |\mathcal{F}\{\mathbf{D}\}|^2} \right\}$   
 $T_t = \gamma^t T_0$   
**if**  $E(\tilde{\mathbf{x}}, \tilde{\boldsymbol{\vartheta}}) \leq E(\mathbf{x}^{(t-1)}, \boldsymbol{\vartheta}^{(t-1)})$  **then**  
 $\boldsymbol{\vartheta}^{(t)} \leftarrow \tilde{\boldsymbol{\vartheta}}$   
**else**  
Draw  $\alpha \sim \mathcal{U}[0, 1]$   
**if**  $\alpha \leq e^{-\frac{E(\tilde{\mathbf{x}}, \tilde{\boldsymbol{\vartheta}}) - E(\mathbf{x}^{(t-1)}, \boldsymbol{\vartheta}^{(t-1)})}{T_t}}$  **then**  
 $\boldsymbol{\vartheta}^{(t)} \leftarrow \tilde{\boldsymbol{\vartheta}}$   
**else**  
 $\boldsymbol{\vartheta}^{(t)} \leftarrow \boldsymbol{\vartheta}^{(t-1)}$   
**end if**  
**end if**  
 $t \leftarrow t + 1$   
**end while**  
**return**  $\boldsymbol{\vartheta}^{(t)}$

---

- 3) Update the pose vector with the Metropolis-Hastings rule for symmetric proposal distributions:

$$\boldsymbol{\vartheta}^{(t)} = \begin{cases} \tilde{\boldsymbol{\vartheta}}, & \text{if } \Delta E \leq 0 \\ \tilde{\boldsymbol{\vartheta}}, & \text{if } \Delta E > 0 \text{ and } \alpha \leq e^{-\frac{\Delta E}{T_t}} \\ \boldsymbol{\vartheta}^{(t-1)}, & \text{else,} \end{cases} \quad (5)$$

where  $\Delta E = (E(\hat{\mathbf{x}}(\tilde{\boldsymbol{\vartheta}}), \tilde{\boldsymbol{\vartheta}}) - E(\hat{\mathbf{x}}(\boldsymbol{\vartheta}^{(t-1)}), \boldsymbol{\vartheta}^{(t-1)}))$ ,  $\alpha \sim \mathcal{U}[0, 1]$ , and  $T_t$  is a temperature parameter.

We now discuss the choice of the main parameters of the algorithm, namely,  $\boldsymbol{\sigma}$  and  $T_t$ , and the computation of  $E(\hat{\mathbf{x}}(\boldsymbol{\vartheta}), \tilde{\boldsymbol{\vartheta}})$ . The temperature  $T_t$  must increase with the iterations to gradually force  $\boldsymbol{\vartheta}^{(t)}$  to be a sample from a distribution concentrated around the maximum of  $p(\mathbf{y}|\boldsymbol{\vartheta})$ . It is known theoretically that a logarithmic increase of  $T_t$  ensures convergence to the global maximum. Here, we choose the much faster exponential rule  $T_t = \gamma^t T_0$ , with  $\gamma = 0.95$ , which has been empirically shown to converge well in other contexts [34]. The standard deviation  $\boldsymbol{\sigma} = (\boldsymbol{\sigma}_r, \boldsymbol{\sigma}_t)$  is composed of the part  $\boldsymbol{\sigma}_r = (\sigma_r, \sigma_r, \sigma_r)$  associated to rotations and the part  $\boldsymbol{\sigma}_t = (\sigma_t, \sigma_t, \sigma_t)$  associated to translations. Its choice determines a trade off between convergence speed and ability to escape from local minima. To handle the many local minima of our problem, we take the large values  $\sigma_r = 50$  and  $\sigma_t = 5$ , to allow for an extensive exploration of the candidate poses. The main computational effort for evaluating the cost function  $E(\hat{\mathbf{x}}(\tilde{\boldsymbol{\vartheta}}), \tilde{\boldsymbol{\vartheta}})$  is found with  $\hat{\mathbf{x}}(\tilde{\boldsymbol{\vartheta}})$ , which amounts to solving Problem (4). We benefit from the property that (4) can be solved analytically. The solution is efficiently computed in the Fourier domain as

$$\hat{\mathbf{x}}(\tilde{\boldsymbol{\vartheta}}) = \mathcal{F}^{-1} \left\{ \frac{\sum_{i=1}^L \mathcal{F}\{\mathbf{H}_{\tilde{\boldsymbol{\vartheta}}_i}^\top \mathbf{y}_{\tilde{\boldsymbol{\vartheta}}_i}\}}{\sum_{i=1}^L |\mathcal{F}\{\mathbf{H}_{\tilde{\boldsymbol{\vartheta}}_i}\}|^2 + \lambda |\mathcal{F}\{\mathbf{D}\}|^2} \right\}. \quad (6)$$

The detailed steps are given in Algorithm 1.

---

**Algorithm 2** Incremental block-coordinate optimization

---

```

 $\vartheta_i^{(1)} = (0, 0, 0), \forall i \in [1, L]$ 
 $m = 1$ 
while stopping criterion not met do
   $l = 2$ 
  while  $l \leq L$  do ▷ Loop on the angles
    if  $m = 1$  then
       $k = l$  ▷ Consider only  $l$  angles
    else
       $k = L$  ▷ Consider all the angles
    end if
     $\vartheta_l^{(m)} \leftarrow \arg \min_{\vartheta_l} \left( \sum_{i=1}^k \|\mathbf{y}_{\vartheta_i} - \bar{\mathbf{H}}_{\vartheta_i} \hat{\mathbf{x}}(\bar{\vartheta})\|_2^2 \right. \\ \left. + \lambda \|\mathbf{D} \hat{\mathbf{x}}(\bar{\vartheta})\|_2^2 \right)$ 
    with  $\bar{\vartheta} = (\vartheta_1^{(m)}, \dots, \vartheta_{l-1}^{(m)}, \vartheta_l, \vartheta_{l+1}^{(m-1)}, \dots, \vartheta_k^{(m-1)})$  ▷ Solve with Algorithm 1
     $l \leftarrow l + 1$ 
  end while
   $m \leftarrow m + 1$ 
end while
return  $\vartheta^{(m)} = (\vartheta_1^{(m)}, \dots, \vartheta_L^{(m)})$ 

```

---

*B. Incremental Block-Coordinate Strategy*

The pose to be estimated in the MCMC approach contains  $6L$  elements, where  $L$  is the number of classes. Typical values for  $L$  range between 5 and 10 in our implementation. To increase the efficiency of the computations even further, we reduce the dimension of the search space with the aid of a block-coordinate approach. Instead of solving (3) jointly for all angles by considering the full pose parameter vector  $\vartheta$ , we successively minimize w.r.t. the pose  $\vartheta_l$  of each particle, the other particles remaining fixed. Every particle pose is visited  $N_{bc}$  times. At the first iteration of the block-coordinate loop, the particles are incrementally introduced in the energy to limit the influence of potentially improper initialization. Accordingly, at iteration  $m$ , the update of the pose of the  $l$ th particle is realized by solving

$$\hat{\vartheta}_l^{(m)} = \arg \min_{\vartheta_l \in \mathbb{R}^6} \sum_{i=1}^k \|\mathbf{y}_{\vartheta_i} - \bar{\mathbf{H}}_{\vartheta_i} \hat{\mathbf{x}}(\bar{\vartheta})\|_2^2 + \lambda \|\mathbf{D} \hat{\mathbf{x}}(\bar{\vartheta})\|_2^2, \quad (7)$$

where  $\bar{\vartheta} = (\vartheta_1^{(m)}, \dots, \vartheta_{l-1}^{(m)}, \vartheta_l, \vartheta_{l+1}^{(m-1)}, \dots, \vartheta_k^{(m-1)})$   
and  $k = \begin{cases} l, & \text{if } m = 1 \\ L, & \text{else.} \end{cases}$

Problem (7) is solved with Algorithm 1. Another advantage of this approach is that the computation (6) of  $\hat{\mathbf{x}}(\bar{\vartheta})$  is facilitated by the fact that only one angle  $\vartheta_l$  is updated at each MCMC iteration. Instead of computing every term of the sums in (6), we only have to update the quantities  $\mathbf{H}_{\vartheta_l}^\top \mathbf{H}_{\vartheta_l}$  and  $\mathbf{H}_{\vartheta_l}^\top \mathbf{y}_{\vartheta_l}$  at each iteration. The incremental block-coordinate strategy is detailed in Algorithm 2.

IV. HIGH-ACCURACY RECONSTRUCTION

Once a first model has been reconstructed, we turn to the high-accuracy mode. This means that we consider the full

complexity of the original problem (2), with neither down-sampling nor reduction of the number of particles. We also set  $p = 1$  in (2) to deploy a total-variation regularization (TV), which is known to improve the quality of image reconstruction by preserving sharp discontinuities. We solve the optimization problem by alternating minimizations w.r.t.  $\mathbf{x}$  with  $\vartheta$  fixed and w.r.t.  $\vartheta$  with  $\mathbf{x}$  fixed. The *reference-free* reconstruction output is likely to initialize the optimization close to the global optimum. We now detail our minimization strategies for the two subproblems.

*A. Minimization w.r.t.  $\mathbf{x}$*

The minimization problem w.r.t.  $\mathbf{x}$  is convex and the forward model is linear. The use of a nonlinear  $\ell_1$  penalty function for the regularization imposes us to resort to an iterative optimization method. The main difficulty comes from the computational cost associated with the large number of particles. In [19], we proposed a proximal splitting framework to deal with this problem for single-channel data and obtained fast and accurate reconstructions. We use the same approach here and apply it to the multichannel model (2).

Many macromolecular assemblies exhibit point group symmetry [44] that can be exploited to improve their reconstruction. Therefore, we also introduce a symmetry constraint whenever this information is available. To this end, we symmetrize the reprojected views according to the considered symmetry group. Since every term involving sums over the views can be pre-computed before the iterative part of the algorithm, the new views do not need to be stored and do not increase significantly the computation time.

*B. Minimization w.r.t.  $\vartheta$*

The minimization of (2) w.r.t.  $\vartheta$  requires the registration of each particle  $\mathbf{y}_{\vartheta_i}$  on the volume  $\mathbf{x}$  convolved with the PSF rotated by  $\vartheta_i$ . The problem is strongly non-convex and we have no prior knowledge about the poses. Therefore, a continuous rigid registration approach with gradient-based optimization would be prone to undesirable local minima. Meanwhile, the MCMC approach of Section III is no longer tractable computationally because of the high dimensionality and size of the data.

Therefore, we have chosen an exhaustive search approach that consists in evaluating the cost function at all points of a discretized space of admissible rotations and translations. The brute force approach to minimize (2) would, however, involve too many time-consuming 3D rotations and convolutions of the input particles with the PSF to evaluate  $\mathbf{y}_{\vartheta_i}$  and  $\mathbf{H}_{\vartheta_i}$ . Instead, we consider the equivalent formulation

$$\hat{\vartheta} = \min_{\vartheta \in \mathbb{R}^{K \times 6}} \sum_{i=1}^K \|\mathbf{y}_i - \bar{\mathbf{H}} \mathbf{x}_{\vartheta_i}\|_2^2, \quad (8)$$

where  $\mathbf{y}_i$  represents the original detected particles,  $\bar{\mathbf{H}}$  represents the non-rotated PSF, and  $\mathbf{x}_{\vartheta_i}$  represents the single volume rotated and translated with the pose  $\vartheta_i$ . With this formulation, we apply the rotations only on the reconstructed model  $\mathbf{x}$  at each point of the discrete parameter space to

create a library of volumes. Each particle is compared to all the elements of the library and is assigned the parameters of the volume that minimizes the cost function. This approach is adapted from the *projection-matching* procedure used in cryo-EM to estimate poses from projections of particles [11].

To speed up the search, we use two strategies:

- We decouple translation and rotation. The best translation is first estimated for a fixed rotation, and the best rotation is then found for the estimated translation. This allows us to reduce the dimensionality of the search space.
- The angular search is realized with a coarse-to-fine scheme. We first perform angular assignments at a coarse angular sampling and we gradually refine the angles around the current value at each iteration.

## V. EXPERIMENTAL RESULTS

### A. Evaluation Protocol

**Simulated Data** To evaluate the performance of our method, we first generated realistic fluorescence imaging data. As a gold standard, we use volumes reconstructed with real data of cryo-EM macromolecular structures, publicly available in the EMDatabank<sup>1</sup> database, which represent the structure of particles at a subnanometer resolution. We use this as ground truth to generate fluorescence measurements in the channel that represents the structure of the particle. As particles, we selected part of the cartwheel of the centriole in *Trichonympha* [23] and a synthesized DNA assembly [45] (red in the figures). To simulate the other channel (shown in green in the figures), we position signals in realistic locations with respect to the structure, as exemplified for the cartwheel of the centriole where the proteins are placed repeatedly at the periphery of the structure (Figure 3). We generate a multichannel volume containing several replicates of the particle with random 3D rotations. We set the size of each particle to  $(45 \times 45 \times 45)$ . This volume is convolved with a PSF, that we chose to be Gaussian in our simulations for simplicity. The standard deviation of the PSF is set to 4 pixels in the lateral plane and 16 pixels in the axial direction, which produces a strong blurring of the particles. Then, we add Gaussian noise to produce the final input volumes, which are shown in Figure 2 with three zoomed in examples of individual particles at different views.

**Comparison With Other Method** The classical approach to improve resolution is to deconvolve a single view. For a fair comparison, we apply our reconstruction method to a set of different particles with the same known orientation, in order to reproduce the noise averaging effect achieved in the presence of many particles. We compare our method with this approach, which we call *single-view*.

**Quantitative Evaluation Metric** The accuracy of reconstruction is measured by the structural similarity index (SSIM) [46], which is defined for two volumes  $\mathbf{x}_1$  and  $\mathbf{x}_2$  by

$$SSIM(\mathbf{x}_1, \mathbf{x}_2) = \frac{(2\mu_1\mu_2 + C_1)(2\sigma_{12} + C_2)}{(\mu_1^2 + \mu_2^2 + C_1)(\sigma_1^2 + \sigma_2^2 + C_2)} \quad (9)$$

where  $\mu_i$  and  $\sigma_i$  are the mean and variance of the volume  $\mathbf{x}_i$ , respectively,  $\sigma_{12}$  is the cross-covariance between the two

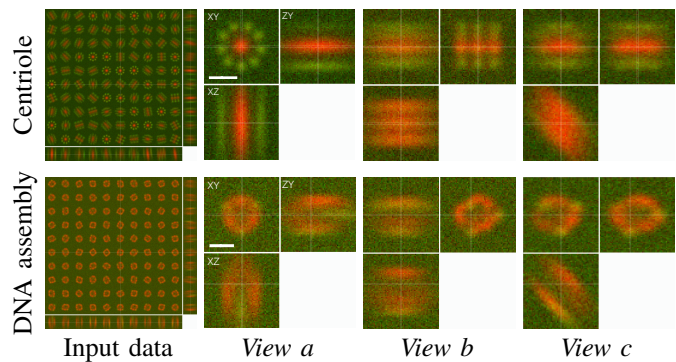


Fig. 2. Simulated input fluorescence volumes from reconstructions in cryo-EM of a portion of the centriolar cartwheel from *Trichonympha* [23] (top row) and a DNA assembly [45] (bottom row). In the left column, we show the input micrographs containing multiple replicates of the particle, and in the other columns three different views extracted from the input micrographs. The scale bar is 50nm for the centriole and 15nm for the DNA assembly.

volumes, and we set the stabilization constants  $C_1 = 0.01$ ,  $C_2 = 0.03$ .

**Implementation Details** We have always optimized the regularization parameter  $\lambda$  in (2) by exhaustive search to maximize the SSIM index. The number of block-coordinate loops is set to  $N_{bc} = 3$ . The MCMC iterations are stopped when the temperature reaches  $T = 10^{-4}$ . Unless stated otherwise, we use 50 particles in the simulated data. The coarse-to-fine angular sampling for the minimization w.r.t.  $\vartheta$  (Section IV-B) is realized in 3 iterations. At the first iteration, the whole space of 3D Euler angles is sampled with a sampling step of 20 degrees. At the second iteration, the angles are discretized around the current estimate in a range of  $[-10, 10]$  degrees, with a sampling step of 5 degrees. At the third iteration, the angles are discretized around the current estimate in a range of  $[-5, 5]$  degrees, with a sampling step of 1 degree. In the clustering operation of the *reference-free* reconstruction, the number of classes  $L$  has to be chosen by the user. It must be high enough to capture most of the structural details of the particle. We set  $L = 5$  for the centriole data and  $L = 10$  for the DNA assembly data. The particle detection step exploits the 2D method implemented in the Scipion software [15]. Specific functions for 3D processing have been implemented in C++ and Python. The classifier is trained with 20 manually picked particles. The detected particles are interpolated with cubic interpolation to reach isotropic sampling. No pre-processing is applied on the detected particles. We implemented the *reference-free* and *high-accuracy* reconstruction steps in MATLAB. The centriole data is known to have a nine-fold axial symmetry, which we exploit by enforcing the symmetry constraint in the reconstruction. The synthesized DNA data does not belong to any symmetry group.

**Visualization** The volumes are visualized both with a 3D model and with orthogonal views. The raw data are only visualized with orthogonal views since the presence of noise is not suitable for 3D representation.

### B. Results on Simulated Data

We show the localization accuracy of our method in Figures 3 and 4 using centriole and DNA assembly data, respec-

<sup>1</sup><http://www.emdatabank.org/search.html>

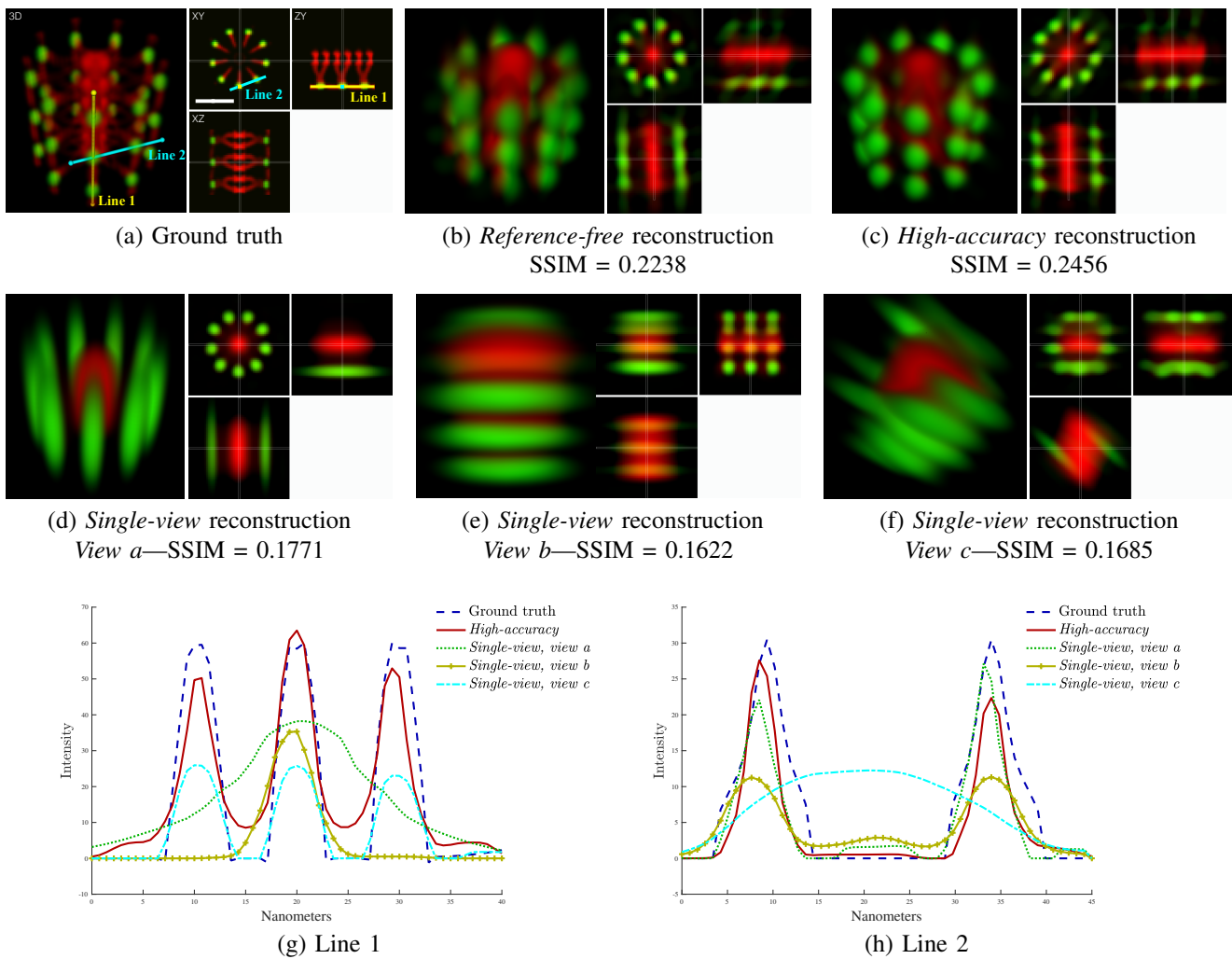


Fig. 3. Results obtained from the centriole data of Figure 2. (a): ground truth; (b-c): *reference-free* and *high-accuracy* steps of our method; (d-f) *single-view* reconstructions from the three views shown in Figure 2. All the particles have been aligned at the same orientation for visualization; (g-h): intensity profiles along Lines 1 and 2, represented on the ground truth (a). The scale bar is 50nm.

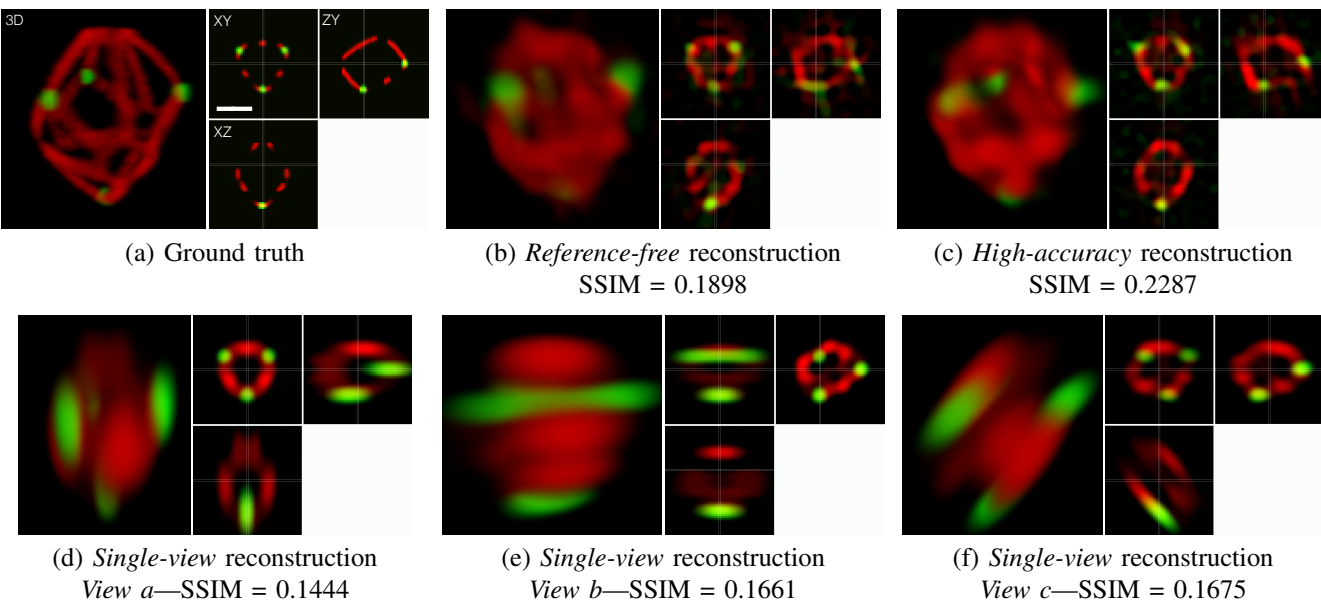


Fig. 4. Results obtained from the DNA assembly data of Figure 2. (a): ground truth; (b-c): *reference-free* and *high-accuracy* steps of our method; (d-f) *single-view* reconstructions from the three views shown in Figure 2. All the particles have been aligned at the same orientation for visualization. The scale bar is 15nm.

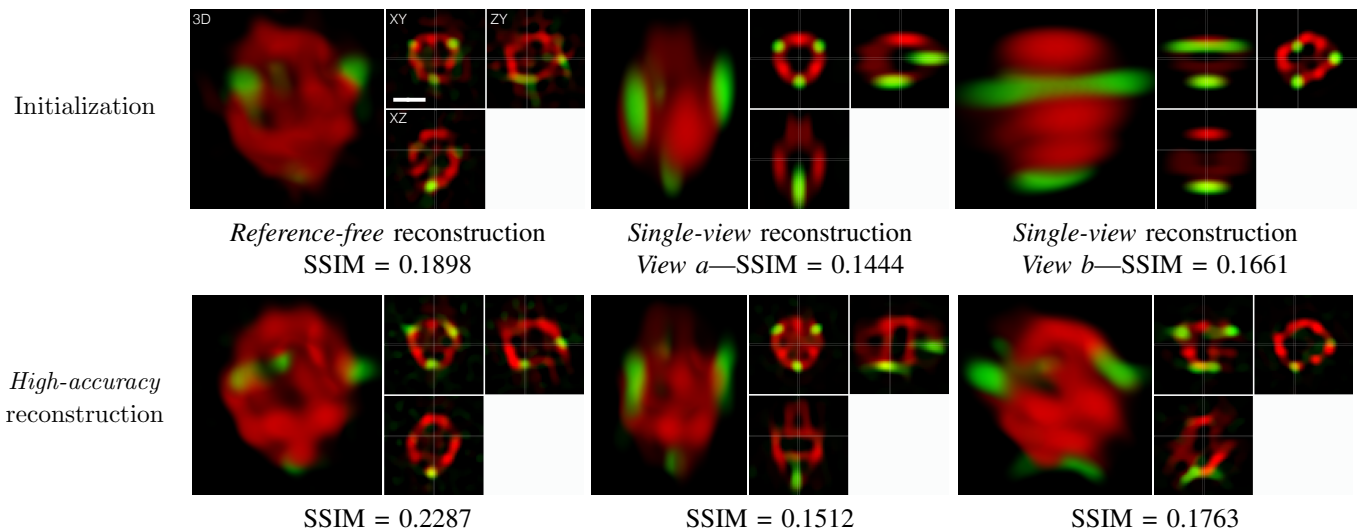


Fig. 5. Comparison of the *high-accuracy* reconstruction (bottom row) obtained with different initializations (top row), with the DNA assembly data: *reference-free* reconstruction (first column) and *single-view* reconstruction with two different orientations (second and third columns). The scale bar is 15nm.

tively. In both figures, we compare our *reference-free* and *high-accuracy* results with the *single-view* approach for three different angles. In Figures 3(g-h), we plot intensity profiles of the reconstructed volumes along two lines represented on the ground truth in Figure 3(a). We consider a line in the XY plane and another one in the ZY plane, and compare our method with the *single-view* results.

We find that the resolution achieved by our method is more isotropic than that one achieved by the *single-view* reconstructions. The improvement is reflected by the SSIM index reported in Figures 3 and 4. We observe in the orthogonal views that the high lateral resolution applies only to one side of the *single-view* reconstructions, whereas it is extended in all directions in our reconstructed model. The 3D localization of proteins inside the centriole structure in Figure 3 is impossible to achieve in any orientation with the *single-view* approach. With our reconstruction, by contrast, the proteins are well separated and can be accurately localized. This is highlighted in Figures 3(g-h), where the *single-view* reconstructions can recover the position of the spheres only in the plane orthogonal to their orientation (*single-view a* recovers the spheres in Line 2 but not in Line 1, and *single-view c* recovers the spheres in Line 1 but not in Line 2). whereas our reconstruction clearly delineates the spheres in both directions. Let us remark that the synthesized DNA data of Figure 4 is much more challenging to handle because of the absence of symmetry. The computational time for the centriole data was  $\sim 5$  minutes for the *reference-free* reconstruction and  $\sim 15$  minutes for the *high-accuracy* reconstruction.

### C. Importance of the Reference-Free Reconstruction

The main advantage of our method is that it does not need to be initialized with a template, which is usually not available with real data. To emphasize the importance of this feature, we compare in Figure 5 the results obtained with our *high-accuracy* reconstruction when it is initialized either by our *reference-free* reconstruction or by the *single-*

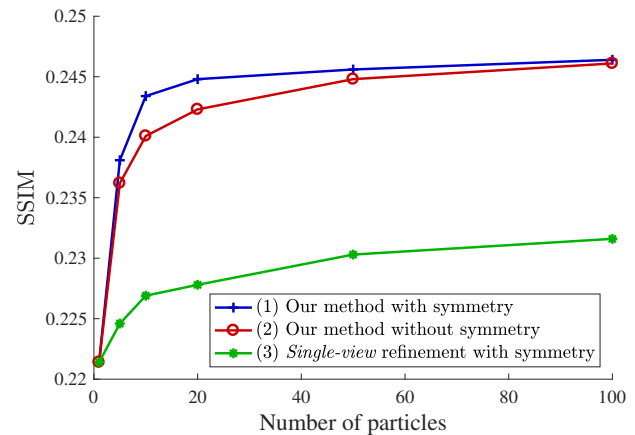


Fig. 6. Plot of the evolution of the reconstruction SSIM with the number of views for our method with symmetry constraint (1), without symmetry constraint (2), and for the refinement of the *single-view* approach with our *high-accuracy* step (3).

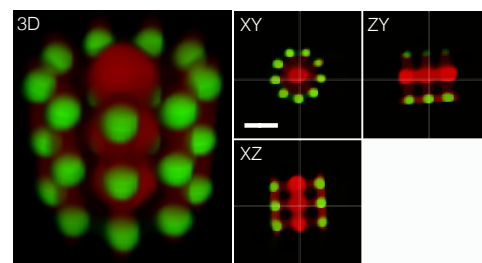


Fig. 7. Volume reconstructed by our method without symmetry constraint, using the centriole data. The scale bar is 50nm.

*view* reconstruction, for two different orientations. We observe that the *high-accuracy* reconstruction is very sensitive to initialization. In particular, it cannot deviate from the oriented blurring of the initialization with the *single-view* reconstruction. Thus, our *reference-free* step—which does not require any initialization—is essential to yield better accuracy, both visually and in terms of SSIM index.

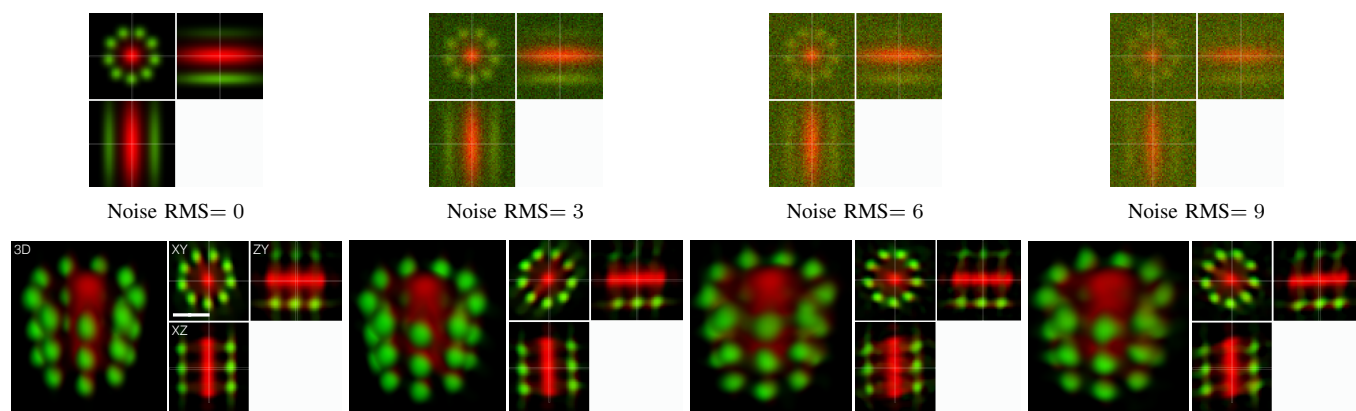


Fig. 8. Reconstruction results with our method (bottom row) for different noise levels in the input volumes. One example of input particle is shown in the top row for each noise level. The ground truth volume have values ranged between 0 and 90, and the noise root mean square (RMS) is indicated in each case. The scale bar is 50nm.

#### D. Impact of the number of particles and the symmetry constraint

In Figure 6, we show how the number of particles in the input volumes influences the SSIM of the reconstructed volume, for the simulated centriole data. We compare three versions of our method: 1) with C9 symmetry constraint; 2) without symmetry constraint; 3) replacing the *reference-free* step by the *single-view* reconstruction (as in Figure 5) and with C9 symmetry constraint. In Figure 7, we show the reconstruction result of our method without symmetry constraint, with 50 input particles.

In all cases, increasing the number of particles improves accuracy. The symmetry constraint improves significantly the results when the number of particles is low, and gradually converges to the same accuracy as the number of particles increases. The visual comparison between the result without symmetry constraint in Figure 6 and the result with symmetry constraint in Figure 3(c) of the article confirms that when the number of particles is sufficiently high, the results are very similar. Thus, the symmetry constraint is particularly useful to reduce the number of particles used for the reconstruction. A lower number of particles facilitates data acquisition and reduces the computational cost.

#### E. Robustness to Noise

In Figure 8, we show reconstructions obtained with our method for different amounts of noise. We observe that the accuracy is only slightly affected by heavy noise in the data.

#### F. Validation on Real Data

To investigate the usefulness of our method on actual experimental data, we acquired STED images of isolated human centrioles in different orientations. Centrioles purified from KE37 cells were spun on coverslips [21], [24], fixed with methanol and immuno-stained with primary antibodies directed against tubulin mono-glutamylated (GT335, Apodigen) and the centriolar protein CEP63, which is known to be present in a torus around the base of mature centrioles (061292, Merck Millipore). Secondary antibodies were anti-mouse ATTO647N (to reveal GT335) and anti-rabbit Alexa594

(to reveal Cep63). STED stacks of 2.19 depth (with 146nm z-step size) with a xy-pixel size of 16nm were acquired on a Leica 3X STED equipped with a 100X 1.4 NA objective. Two-color stacks were acquired by sequential excitation at 594nm and 646nm using the same STED depletion Laser at 775nm, with time gated acquisition to improve the signal to noise ratio. The PSF was estimated by separately imaging 20nm diameter fluorescent nanospheres (FluoSpheres) spun on a coverslip and imaged separately. Since the centriole displays nine-fold symmetry, we applied a C9 symmetry constraint on the reconstruction, as in the case of our first simulated data set. Note that due to their cylindrical shape, the centrioles tend to favor top and side orientations in the input data (see Figures 9(b) and 9(c)). While this breaks the assumption of isotropy of the orientations that we made in Section II-A, these two tilt orientations capture most of the information in the specific case of cylindrical organization of the structure. Accordingly, we set  $L = 2$  in the *reference-free* reconstruction, which led to classes corresponding to top and side views.

In Figure 9(a), we show an example of multichannel input volume, zoomed in on two particles that we call “View a” and “View b” in Figures 9(b)-(c). The entire input data is composed of 6 samples similar to the one of Figure 9(a). In Figure 9(d) we show the volume reconstruction that we obtained with our method. We compare the result of our method with the *Single-view* reconstruction of “View a” and “View b” in Figures 9(e)-(f). In Figure 10, we determine with precision the shape and localization of Cep63 and tubulin in the centriole based on our reconstruction of Figure 9(d).

While the position and the shape is murky with the *single-view* reconstructions, the isotropic reconstruction from several views clearly reveals in 3D the exact position of Cep63 around mono-glutamylated tubulin that marks the microtubule wall of the centriole. Note that the resolution of the input STED volumes is too low to make the C9 symmetry appear in the reconstruction. The reconstruction reveals that the glutamylated tubulin staining forms a cylinder 400nm in height and 176nm in diameter, fitting with the dimension observed for the human centriole using electron microscopy [35]. The red channel reveals that Cep63 forms a torus around the glutamylated

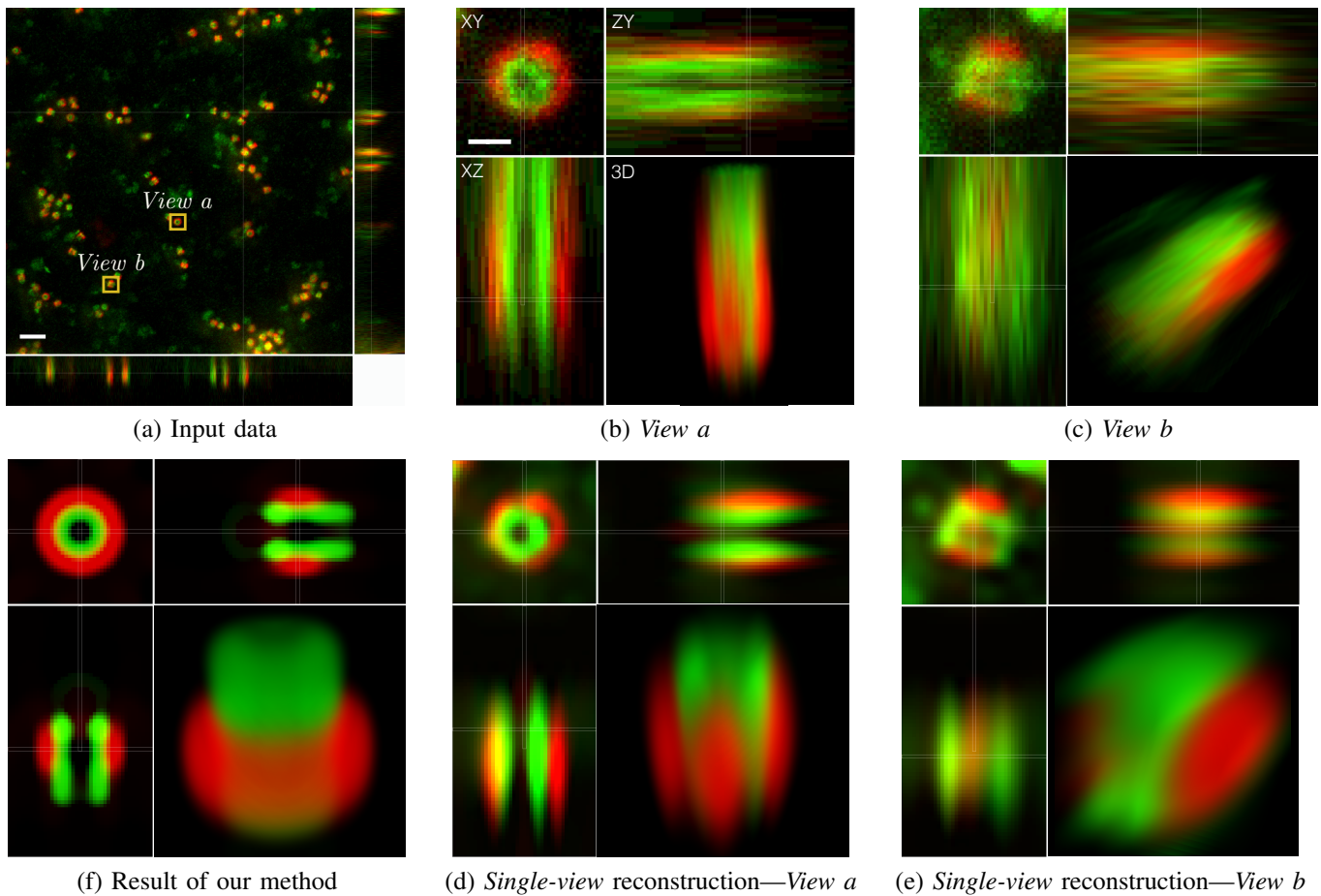


Fig. 9. Single volume reconstruction on real centriole data labelled to reveal the protein CEP63 and tubulin mono-glutamylation. (a): one of the input volumes; (b)-(c) zoomed in visualizations of two particles, *View a* and *View b*; (d): reconstructed model with our method; (e)-(f): reconstructions obtained with the *single-view* approach for *View a* and *View b*. The scale bar is  $1.25\mu\text{m}$  on figure (a) and  $190\text{nm}$  on figure (b).

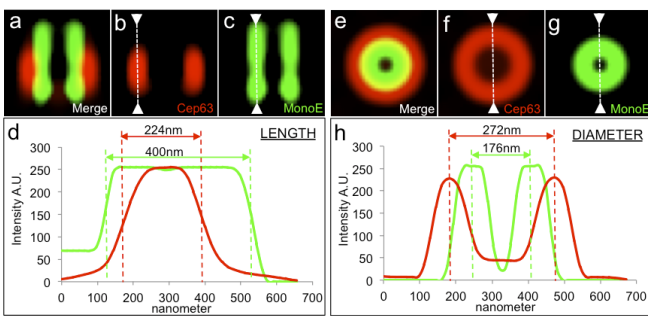


Fig. 10. Quantitative characterization of the shape and localization of CEP63 (red) and tubulin (green) with our reconstructed single volume (Figure 9 (d)).

tubulin channel with a height of  $224\text{nm}$  and a diameter of  $272\text{nm}$  (Figure 10). In addition, this reconstruction reveals that Cep63 is not decorating the utmost proximal region of the centriole, as expected, but instead starts at  $\sim 50\text{nm}$  above the proximal ends. This suggests a tighter spatial localization than previously reported [32].

## VI. CONCLUSION – PERSPECTIVES

We have presented a new computational method to localize proteins and other sub-macromolecular components using

multichannel fluorescence microscopy. We proposed a framework where we perform semi-automatic particle detection, orientation estimation, and single volume reconstruction. To reconstruct isotropic volumes, we applied this method on samples that contain several replicates of a macromolecule with different orientations. We formulated the major issue of joint orientation estimation and single volume reconstruction as a non-convex optimization problem without initial reference. We reformulated the problem as a bilevel optimization that we solve with a stochastic optimization approach. To ensure computational tractability, we proposed an adaptive complexity reduction and an incremental block-coordinate strategy. We showed that the localization of proteins or other sub-macromolecular components into 3D macromolecular assemblies is made possible by the isotropic resolution achieved by our method, whereas it cannot be achieved with the classical *single-view* approach. Furthermore, we showed the practical potential of our method on real data by uncovering the precise isotropic localization of Cep63 around mono-glutamylated microtubules that mark the centriolar barrel.

Our method opens several perspectives of extension. The main research directions for future work can be summarized as follows:

- The detection step could be improved by adapting the

increasingly popular deep learning approaches from computer vision [39].

- The framework could be extended to imaging modalities that are not based on a convolutive forward model, like SMLM imaging. While the bilevel MCMC framework of the *reference-free* step and the alternated optimization of the *high-accuracy* step are generic, the volume reconstruction task (minimization of (2) w.r.t.  $x$ ) needs to be adapted to each new modality.
- Our model assumes Gaussian noise in the input data for simplicity. Considering Poisson noise would be more realistic for fluorescence imaging. This would require the adaptation of the volume reconstruction step to data terms with Kullback-Leibler penalty function. Solutions for this problem have been investigated for deconvolution in proximal splitting frameworks [18], [30], which could be applied to our case.
- Our assumption of identical particles can be violated in case of imperfect fluorescent labelling. While this approximation is sufficient for our STED data with C9 symmetry, it can become a limitation in other cases, in particular for SMLM methods. We are currently developing extensions of our method to handle this situation.

The mapping of Cep63 in the centriole presented in Section V-F is a first step to establish a precise cartography of sub-macromolecular components within the centriole. The next step is to investigate the robustness of our method when applied to different particle shapes. Our long term goal is to complete the cartography of the centriole, and generalize it to other large macromolecular complexes.

## REFERENCES

- [1] V. Abrishami, A. Zaldívar-Peraza, J. M. de la Rosa-Trevín, J. Vargas, J. Otón, R. Marabini, Y. Shkolnisky, J. M. Carazo, and C. O. S. Sorzano. A pattern matching approach to the automatic selection of particles from low-contrast electron micrographs. *Bioinformatics*, pages 4–29, 2013.
- [2] B. M. T. Acosta, P. Bouthemy, and C. Kervrann. A common image representation and a patch-based search for correlative light-electron-microscopy (CLEM) registration. In *International Symposium on Biomedical Imaging (ISBI)*, Prague, Czech Republic, 2016.
- [3] J.-C. Baritoux, K. Hassler, and M. Unser. An efficient numerical method for general  $\ell_p$  regularization in fluorescence molecular tomography. *IEEE Transactions on Medical Imaging*, 29(4):1075–1087, 2010.
- [4] D. P. Bertsekas. *Nonlinear programming*. Athena scientific Belmont, 1999.
- [5] E. Betzig, G. Patterson, R. Sougrat, O. Lindwasser, S. Olenych, J. Bonifacino, M. Davidson, J. Lippincott-Schwartz, and H. Hess. Imaging intracellular fluorescent proteins at nanometer resolution. *Science*, 313(5793):1642–1645, 2006.
- [6] S. Bhat, I. V. Larina, K. V. Larin, M. E. Dickinson, and M. Liebling. 4D reconstruction of the beating embryonic heart from two orthogonal sets of parallel optical coherence tomography slice-sequences. *IEEE Transactions on Medical Imaging*, 32(3):578–588, 2013.
- [7] J. Boulanger, C. Gueudry, D. Münch, B. Cinquin, P. Paul-Gilloteaux, S. Bardin, C. Guérin, F. Senger, L. Blanchoin, and J. Salamero. Fast high-resolution 3D total internal reflection fluorescence microscopy by incidence angle scanning and azimuthal averaging. *Proceedings of the National Academy of Sciences*, 111(48):17164–17169, 2014.
- [8] J. Broeken, H. Johnson, D. Lidke, S. Liu, R. Nieuwenhuizen, S. Stallinga, K. Lidke, and B. Rieger. Resolution improvement by 3D particle averaging in localization microscopy. *Methods and Applications in Fluorescence*, 3(1):014003, 2015.
- [9] S. Burns, J. S. Avena, J. R. Unruh, Z. Yu, S. E. Smith, B. D. Slaughter, M. Winey, and S. L. Jaspersen. Structured illumination with particle averaging reveals novel roles for yeast centrosome components during duplication. *eLife*, 4:e08586, 2015.
- [10] T. Cao, C. Zach, S. Modla, D. Powell, K. Czymmek, and M. Niethammer. Multi-modal registration for correlative microscopy using image analogies. *Medical Image Analysis*, 18(6):914–926, 2014.
- [11] J. Carazo, C. O. S. Sorzano, J. Oton, R. Marabini, and J. Vargas. Three-dimensional reconstruction methods in single particle analysis from transmission electron microscopy data. *Archives of Biochemistry and Biophysics*, 581:39–48, 2015.
- [12] K. G. Chan and M. Liebling. A point-spread-function-aware filtered backprojection algorithm for focal-plane-scanning optical projection tomography. In *International Symposium on Biomedical Imaging (ISBI)*, pages 253–256, Prague, Czech Republic, 2016.
- [13] G. Crivat and J. W. Taraska. Imaging proteins inside cells with fluorescent tags. *Trends in biotechnology*, 30(1):8–16, 2012.
- [14] P. de Boer, J. P. Hoogenboom, and B. N. Giepmans. Correlated light and electron microscopy: ultrastructure lights up! *Nature methods*, 12(6):503–513, 2015.
- [15] J. M. de la Rosa-Trevín, A. Quintana, L. Del Cano, A. Zaldívar, I. Foche, J. Gutiérrez, J. Gómez-Blanco, J. Burguet-Castell, J. Cuenca-Alba, V. Abrishami, J. Vargas, J. Otón, G. Sharov, J. L. Vilas, J. Navas, P. Conesa, M. Kazemi, C. O. S. Sorzano, and J. M. Carazo. Scipion: A software framework toward integration, reproducibility and validation in 3D electron microscopy. *Journal of Structural Biology*, 2016.
- [16] L. Denis, E. Thiébaud, F. Soulez, J.-M. Becker, and R. Mourya. Fast approximations of shift-variant blur. *International Journal of Computer Vision*, 115(3):253–278, 2015.
- [17] N. Dey, L. Blanc-Feraud, C. Zimmer, P. Roux, Z. Kam, J.-C. Olivo-Marin, and J. Zerubia. Richardson-Lucy algorithm with total variation regularization for 3d confocal microscope deconvolution. *Microscopy Research and Technique*, 69(4):260–266, 2006.
- [18] M. Figueiredo and J. Bioucas-Dias. Restoration of {Poissonian images using alternating direction optimization. *IEEE Transactions on Image Processing*, 19(12):3133–3145, 2010.
- [19] D. Fortun, P. Guichard, N. Chu, and M. Unser. Reconstruction from multiple poses in fluorescence imaging: Proof of concept. *IEEE Journal of Selected Topics in Signal Processing*, 10(1):61–70, 2016.
- [20] S. Geman and D. Geman. Stochastic relaxation, Gibbs distributions, and the Bayesian restoration of images. *IEEE Transactions on Pattern Analysis and Machine Intelligence*, (6):721–741, 1984.
- [21] D. Gogondeau, P. Guichard, and A.-M. Tassin. Purification of centrosomes from mammalian cell lines. *Methods in cell biology*, 129:171–189, 2015.
- [22] M. Gu. *Advanced optical imaging theory*, volume 75. Springer Science & Business Media, 2000.
- [23] P. Guichard, V. Hachet, N. Majubu, A. Neves, D. Demurtas, N. Olieric, I. Fluckiger, A. Yamada, K. Kihara, Y. Nishida, S. Moriya, M. Steinmetz, Y. Hongoh, and P. Gönczy. Native architecture of the centriole proximal region reveals features underlying its 9-fold radial symmetry. *Current Biology*, 23(17):1620–1628, 2013.
- [24] V. Hamel, P. Guichard, M. Fournier, R. Guet, I. Fluckiger, A. Seitz, and P. Gonczy. Correlative multicolor 3D SIM and STORM microscopy. *Biomedical Optics Express*, 5(10):3326–3336, 2014.
- [25] X. Heiligenstein, J. Heiligenstein, C. Delevoeye, I. Hurbain, S. Bardin, P. Paul-Gilloteaux, L. Sengmanivong, G. Régnier, J. Salamero, C. Antony, and G. Raposo. The cryocapsule: simplifying correlative light to electron microscopy. *Traffic*, 15(6):700–716, 2014.
- [26] B. Huang, W. Wang, M. Bates, and X. Zhuang. Three-dimensional super-resolution imaging by stochastic optical reconstruction microscopy. *Science*, 319(5864):810–813, 2008.
- [27] T. A. Klar, S. Jakobs, M. Dyba, A. Egner, and S. W. Hell. Fluorescence microscopy with diffraction resolution barrier broken by stimulated emission. *Proceedings of the National Academy of Sciences*, 97(15):8206–8210, 2000.
- [28] G. Knott and C. Genoud. Is EM dead? *J Cell Sci*, 126(20):4545–4552, 2013.
- [29] W. Kukulski, M. Schorb, S. Welsch, A. Picco, M. Kaksonen, and J. Briggs. Precise, correlated fluorescence microscopy and electron tomography of lowicryl sections using fluorescent fiducial markers. *Methods in Cell Biology*, 111:235–257, 2011.
- [30] S. Lefkimmiatis, J. Ward, and M. Unser. Hessian Schatten-norm regularization for linear inverse problems. *IEEE Transactions on Image Processing*, 22(5):1873–1888, May 2013.
- [31] A. Löschberger, S. van de Linde, M. Dabauvalle, B. Rieger, M. Heilemann, G. Krohne, and M. Sauer. Super-resolution imaging visualizes the eightfold symmetry of gp210 proteins around the nuclear pore complex and resolves the central channel with nanometer resolution. *Journal of Cell Science*, 125(3):570–575, 2012.

- [32] G. Lukinavicius, D. Lavogina, M. Orpinell, K. Umezawa, L. Reymond, N. Garin, P. Gönczy, and K. Johnsson. Selective chemical crosslinking reveals a cep57-cep63-cep152 centrosomal complex. *Current Biology*, 23(3):265–270, 2013.
- [33] V. Mennella, B. Keszthelyi, K. McDonald, B. Chhun, F. Kan, G. Rogers, B. Huang, and D. Agard. Subdiffraction-resolution fluorescence microscopy reveals a domain of the centrosome critical for pericentriolar material organization. *Nature Cell Biology*, 14(11):1159–1168, 2012.
- [34] Y. Nourani and B. Andresen. A comparison of simulated annealing cooling strategies. *Journal of Physics A: Mathematical and General*, 31(41):8373, 1998.
- [35] M. Paintrand, M. Moudjou, H. Delacroix, and M. Bornens. Centrosome organization and centriole architecture: their sensitivity to divalent cations. *Journal of structural biology*, 108(2):107–128, 1992.
- [36] S. R. P. Pavani, M. A. Thompson, J. S. Biteen, S. J. Lord, N. Liu, R. J. Twieg, R. Piestun, and W. Moerner. Three-dimensional, single-molecule fluorescence imaging beyond the diffraction limit by using a double-helix point spread function. *Proceedings of the National Academy of Sciences*, 106(9):2995–2999, 2009.
- [37] M. Pereyra, P. Schniter, E. Chouzenoux, J.-C. Pesquet, J.-Y. Tourneret, A. O. Hero, and S. McLaughlin. A survey of stochastic simulation and optimization methods in signal processing. *IEEE Journal of Selected Topics in Signal Processing*, 10(2):224–241, 2016.
- [38] S. Preibisch, F. Amat, E. Stamatakis, M. Sarov, R. Singer, E. Myers, and P. Tomancak. Efficient {Bayesian-based multiview deconvolution. *Nature Methods*, 11(6):645–648, 2014.
- [39] S. Ren, K. He, R. Girshick, and J. Sun. Faster r-cnn: Towards real-time object detection with region proposal networks. In *Advances in neural information processing systems*, pages 91–99, 2015.
- [40] M. J. Rust, M. Bates, and X. Zhuang. Sub-diffraction-limit imaging by stochastic optical reconstruction microscopy (storm). *Nature methods*, 3(10):793–796, 2006.
- [41] K. Sonnen, L. Schermelleh, H. Leonhardt, and E. Nigg. 3D-structured illumination microscopy provides novel insight into architecture of human centrosomes. *Biology Open*, 1(10):965–976, 2012.
- [42] A. Szymborska, A. de Marco, N. Daigle, V. Cordes, J. Briggs, and J. Ellenberg. Nuclear pore scaffold structure analyzed by super-resolution microscopy and particle averaging. *Science*, 341(6146):655–658, 2013.
- [43] M. Temerinac-Ott, O. Ronneberger, P. Ochs, W. Driever, T. Brox, and H. Burkhardt. Multiview deblurring for 3-d images from light-sheet-based fluorescence microscopy. *IEEE Transactions on Image Processing*, 21(4):1863–1873, 2012.
- [44] B. Vainshtein. Symmetry of biological macromolecules and their associations. *Computers & Mathematics with Applications*, 12(1-2):237–269, 1986.
- [45] R. Veneziano, S. Ratanalert, K. Zhang, F. Zhang, H. Yan, W. Chiu, and M. Bathe. Designer nanoscale dna assemblies programmed from the top down. *Science*, pages 43–88, 2016.
- [46] Z. Wang, A. C. Bovik, H. R. Sheikh, and E. P. Simoncelli. Image quality assessment: from error visibility to structural similarity. *IEEE Transactions on Image Processing*, 13(4):600–612, 2004.
- [47] W. I. Zangwill. Nonlinear programming: a unified approach. 1969.